Journal of
Engineering Sciences
Faculty of Engineering
Assiut University
JES
مجلة
العلوم الهندسية
كلية الهندسة
جامعة أسيوط
journal homepage: http://jesaun.journals.ekb.eg

# Numerical Investigation of Film Cooling Effectiveness and Flow Field Characteristics over a Flat Plate with in-Hole Swirl Generator

Received 9 July 2023; Revised 26 September 2023; Accepted 26 September 2023

**A. Ibrahim[1 a],**
**O. Hassan[2a],**
**M. F.F. El-Dosoky[3a, b],**
**M. M. Abdelghany[4a]**

**Keywords**
Film Cooling,
Swirling Coolant Flow,
CRVP,
Vortex Reconstruction,
Blade-type Swirl Generator

**Abstract**
The performance of a new film cooling scheme has been numerically investigated. The scheme consists of a blade-type swirl generator that adds a swirl pattern to the injected coolant stream. Reynolds-Averaged Navier-Stokes equations along with a realizable k-ε turbulence model have been solved. The film cooling effectiveness over a flat plate downstream the coolant injection hole was determined for different generator geometric parameters and operating conditions. These parameters are the generator length to the injection hole diameter ratio, twist angle, and location from the hole inlet. The operating conditions are four different blowing ratios, constant density ratio of 2.0, mainstream turbulence intensity of 5% and Reynolds number of 80,000 based on the hole diameter and mainstream velocity. The results showed an enhancement in the laterally averaged cooling effectiveness accompanied by enriched jet spreading downstream the in-hole swirl generator, while the area-averaged cooling effectiveness increased by 74%, 293%, and 805% at blowing ratios 1.0, 1.5 and 2.0, respectively, compared to that for a scheme without swirl generator. Such enhancement is attributed to the vortical structure generated and hence the interaction with the mainstream. Optimization was conducted on obtained results to determine the optimal swirl generator geometric parameters.

## Nomenclature

| | |
|---|---|
| $A_m$ | Inlet cross-sectional area of mainstream, mm$^2$ |
| $Ap$ | Inlet cross-sectional area of the plenum, mm$^2$ |
| $CUC$ | Cooling uniformity coefficient, $CUC = 1 - \frac{\lvert\bar{\eta}-\eta_c\rvert}{\eta_c}$ |
| $C_d$ | Discharge coefficient, $C_d = \frac{Actual\ mass\ flowrate}{Ideal\ mass\ flowrate}$ |

[1] Department of Mechanical Engineering, Assiut University, Assiut, Egypt
[2] Department of Mechanical Engineering, Assiut University, Assiut, Egypt
[3] Department of Mechanical Engineering, Assiut University, College of Engineering, Fahad Bin Sultan University
[4] Department of Mechanical Engineering, Assiut University, Assiut, Egypt

https://doi.org/ 10.21608/JESAUN.2023.221981.1244

| | |
|---|---|
| $D$ | Diameter of film cooling hole, mm |
| $DR$ | Density ratio, $DR = \frac{\rho_c}{\rho_m}$ |
| $F_{Cor}$ | Coriolis Force, N |
| $L/D$ | Film cooling hole path length to diameter ratio |
| $L_s/D$ | Swirl generator length to diameter ratio |
| $M$ | Blowing ratio, $M = \frac{\rho_c v_c}{\rho_m v_m}$ |
| $P_i$ | Total pressure at certain point $i = 1, 2, ..$ , [Pa] |
| $P/D$ | Hole spacing to film cooling hole diameter ratio |
| $Re$ | Reynolds Number, $Re = \frac{v_m * D}{\nu} = 80{,}000$ |
| $S$ | Swirl parameter, $S = \frac{u_\theta}{u_{axial}}$ |
| $SP$ | Swirl generator position inside film cooling hole path measured from path entrance, mm |
| $T_{aw}$ | Adiabatic wall temperature of flat plate wall, K |
| $T_c$ | Coolant air inlet temperature, K |
| $T_m$ | Mainstream inlet temperature, K |
| $u_\theta$ | Circumferential velocity of swirling coolant flow, m/s |
| $u_{axial}$ | Axial velocity of swirling coolant flow, m/s |
| $V$ | Vector of fluid relative velocity, m/s |
| $v_c$ | Coolant air average velocity based on circular hole cross-section area, m/s |
| $v_m$ | Mainstream average inlet velocity, m/s |
| $X$ | Streamwise coordinates, m |
| $Y$ | Vertical coordinates, m |
| $Z$ | Spanwise coordinates, m |
| $\alpha$ | Inclination angle of film cooling hole path, deg |
| $\beta$ | Twist angle of swirl generator, deg |
| $\eta$ | Adiabatic film cooling effectiveness, $\eta = \frac{T_m - T_{aw}}{T_m - T_c}$ |
| $\bar{\eta}$ | Laterally averaged effectiveness, $\bar{\eta} = \frac{1}{3D}\int_{-1.5D}^{1.5D} \eta(X, Z)dz$ |
| $\omega$ | Vector of angular velocity, rad/s |
| $\omega_x$ | Vorticity of x-axis, rad/s |
| $\rho$ | Fluid density, kg/m$^3$ |
| $\rho_c$ | Coolant air density, kg/m$^3$ |
| $\rho_m$ | Mainstream air density, kg/m$^3$ |

**Abbreviations**

| | |
|---|---|
| AM | Additive Manufacturing |
| CRVP | Counter-Rotating Vortex Pair |
| LES | Large Eddy Simulation |
| LIF | Laser Induced Fluorescence |
| PSP | Pressure Sensitive Paint |
| SG | Swirl Generator |
| TET | Turbine Entry Temperature |

## 1. Introduction

Film cooling is an effective cooling technique in gas turbines to retain the durability of vanes and blades in the first stage of the turbine. More research and development in cooling technology will enable turbine designers and manufacturers to get higher firing temperatures and higher Turbine Entry Temperatures (TET) which will reflect on turbine efficiency enhancement, Acharya and Kanani[1]. In film cooling, relatively cooled air is injected close to the external surface of the vanes and blades to make a very thin protective layer of the coolant. The coolant air is extracted from a high-pressure compressor stage. Despite the crucial role of film cooling in gas turbine development there are few drawbacks of such technology. Some of those drawbacks are related to manufacturing limitations, and others are related to the complex phenomena that occur when the coolant jet crosses the mainstream and interacts with it. Several studies have been conducted in the film cooling area. Goldstein [2] reviewed the early works carried out in this area and performed the first film cooling analysis,, while Bunker [3] reviewed film cooling from shaped holes. Bogard and Thole [4] reviewed more recent works and presented a table that summarizes the various parameters considered in those research studies.

As indicated by Leylek et al.[5], in film cooling from a cylindrical hole a Counter Rotating Vortex Pair (CRVP, also called kidney-shaped vortex) rises at a blowing ratio of about 2.0, which leads to effectiveness decay downstream of the cooling hole. Many studies were conducted to investigate the CRVP with two main objectives. The first one is to visualize and understand the structure of CRVP as presented by Fric and Roshko [6], Haven and Kurosaka [7]. The second main objective is to control the CRVP intensity and enhance the film cooling performance by proposing new techniques and modification of existing ones. Kusterer et al. [8] suggested the use of a double-jet scheme, while Heidmann and Ekkad [9] and Dhungel et al. [10] proposed the use of supplemented anti-vortex hole. Ely and Jubran [11, 12] suggested the use of sister holes to generate new vortices that cancel the effect of CRVP, while Li and Hassan [13] proposed the use of a nozzle scheme. All the novel schemes proposed to control CRVP postulated that the performance of film cooling is enhanced by decreasing the intensity of CRVP.

Recently, researchers have considered the reconstruction of vortices by using swirling coolant flow. Kuya et al. [14] used a twisted tape inside the cylindrical hole and found that the performance of film cooling was enhanced due to the generated swirling coolant flow. Several new ideas have been proposed and developed to utilize the benefit of swirling coolant flow. Takeishi et al. [15] developed a new approach to generate swirling coolant flow inside a hexagonal plenum from two inclined staggered impingement jets. They used a Pressure Sensitive Paint (PSP) to measure film cooling effectiveness on a flat plate wall in a low-speed wind tunnel. In addition to that, they used Laser-Induced Fluorescence (LIF) and Particle Image Velocimetry (PIV) to capture the film cooling

effectiveness spatial distribution and flow field, respectively for film cooling from circular and shaped holes. For circular hole, they controlled the swirl strength by changing the angle of the impinging jet from $0° \; to \; 40°$ . The highest film cooling effectiveness obtained was about 0.6 at nozzle angle $30°$ , and $M = 1.0$. Moreover, they postulated that both jet penetration and the generation of CRVP were suppressed by the swirling coolant jet. Besides, the jet deflection was in the direction where the swirling velocity component in the z-direction was positive. Hence, they concluded that the swirling coolant flow can drastically improve film cooling performance. Oda et al. [16] conducted a Large Eddy Simulation (LES) of film cooling with the swirling coolant flow for a circular hole, and they confirmed that the swirling coolant jet was effective in reducing the net heat transfer from the harsh main stream to the vane wall.

Yang et al. [17] studied experimentally the combined effect of the upstream ramp and swirling coolant flow using two impingement jets in the plenum to generate swirling in either a clockwise or counterclockwise direction. They postulated that film cooling coverage downstream the hole was higher in the case of large slant angle of the ramp, than the case of small angle. They attributed that to the suppression of the recirculation vortex induced by the ramp at large angle due to the presence of swirling flow. In addition, they found that the rotation direction of the swirling coolant flow enhances the right and left mixing of CRVP, respectively. Finally, they concluded that combination of cooling structures of ramp and swirling flow resulted in better cooling performance than the singular swirling structure. Yang et al. [18] conducted a numerical investigation of the swirling coolant flow effect on film cooling performance for three different hole geometries. They concluded that a suitable implementation of the swirling coolant flow could enhance film cooling performance for each of three types of holes geometries. Furthermore, they indicated that the film cooling effectiveness for symmetrical cooling configuration was affected by swirling strength of the coolant jet not the swirling direction. On the other hand, the cooling performance for asymmetric cooling configuration was affected by swirling strength and direction similar to the case of compound angle injection. Thurman et al. [19] proposed film cooling from a spiral hole scheme and found that the proposed scheme induces large-scale vorticity which cancels out the CRVP and enhances film cooling performance compared with that of a smooth cylindrical hole scheme. Yue et al. [20] conducted a numerical investigation of three suggested configurations of coolant chambers, all of them use cylindrical holes, to develop swirling coolant flow and new vortex structure. They indicated that increasing the blowing ratio for one of the suggested configurations enhances film cooling performance and induces a unidirectional vortex leading to good adhesion of the coolant jet to the wall. A recent study conducted by Jia et al. [21] investigated numerically a new spiral hole design and compared it to cylindrical hole. They postulated that the averaged film cooling effectiveness of spiral hole is considerably improved compared to cylindrical hole. Furthermore, they obtained a lateral area coverage three times larger than that of a cylindrical hole and this is due to larger lateral-velocity and low momentum at the hole exit.

As indicated in the above discussion, The literature shows few studies that investigated the effect of swirling coolant flow on the film cooling performance. To the authors' knowledge, most of those studies proposed to induce the swirling motion inside the plenum and others suggested to generate swirling flow by changing the hole geometry. While in the present study, a novel scheme is proposed to use a blade-type swirl generator inside the hole path. The present study provides a new design of swirl film cooling configurations exploiting the advantages of swirling coolant flow stated in the literature. The proposed scheme is expected to produce higher laterally averaged film cooling effectiveness and consequently ensure high coverage compared to other schemes. Such wide or high

coverage will be useful in increasing the hole spacing and consequently using a smaller number of holes thus maintaining good structural integrity of turbine blades and vanes which is one of the main challenges to turbine designers. Finally, the new scheme can be manufactured by Additive Manufacturing (AM) that provides design flexibility.

## 2. Numerical method

### 2.1.Governing equations

The simulation of the steady, three dimensional, turbulent, and compressible flow is considered. The flow is governed by the Reynolds Averaged Navier-Stokes (RANS) equations closed by the realizable k-ε turbulence model as follow[22]:

The continuity:

$$\frac{\partial \bar{\rho}}{\partial t} + \frac{\partial}{\partial x_j}\left[\bar{\rho}\bar{u}_j\right] = 0 \tag{1}$$

The momentum:

$$\frac{\partial}{\partial t}\left[\bar{\rho}\bar{u}_i\right] + \frac{\partial}{\partial x_j}\left[\bar{\rho}\bar{u}_i\bar{u}_j + p\delta_{ij} - \left(\bar{\tau}_{ij}{}^{turb} + \bar{\tau}_{ij}{}^{lam}\right)\right] = 0 \tag{2}$$

The energy:

$$\frac{\partial}{\partial t}\left[\bar{\rho}\bar{e}_o\right] + \frac{\partial}{\partial x_j}\left[\bar{\rho}\bar{u}_i\bar{e}_o + \bar{u}_j p - \bar{u}_i\left(\bar{\tau}_{ij}{}^{turb} + \bar{\tau}_{ij}{}^{lam}\right)\right] - \frac{\partial}{\partial x_j}\left[K_{eff}\frac{\partial \bar{\mathrm{T}}}{\partial x_j}\right] = 0 \tag{3}$$

Where: $\bar{\tau}_{ij}{}^{lam} = \mu\left(\frac{\partial \bar{u}_i}{\partial x_j} + \frac{\partial \bar{u}_j}{\partial x_i} - \frac{2}{3}\frac{\partial \bar{u}_k}{\partial x_k}\delta_{ij}\right)$ , $\bar{\tau}_{ij}{}^{turb} = \mu_t\left(\frac{\partial \bar{u}_i}{\partial x_j} + \frac{\partial \bar{u}_j}{\partial x_i} - \frac{2}{3}\frac{\partial \bar{u}_k}{\partial x_k}\delta_{ij}\right) - \frac{2}{3}\bar{\rho}k\delta_{ij}$ and $K_{eff} = C_p\frac{\mu}{Pr} + C_p\frac{\mu_t}{Pr_t}$

The turbulent kinetic energy:

$$\frac{\partial \rho \mathrm{k}}{\partial t} + \bar{u}_j\frac{\partial \rho \mathrm{k}}{\partial x_j} = \frac{\partial}{\partial x_j}\left[\left(\mu + \frac{\mu_t}{\sigma_k}\right)\frac{\partial \mathrm{k}}{\partial x_j}\right] + \mathrm{P}_k - \rho\varepsilon \tag{5}$$

The turbulence dissipation rate:

$$\frac{\partial \rho\varepsilon}{\partial t} + \bar{u}_j\frac{\partial \rho\varepsilon}{\partial x_j} = \frac{\partial}{\partial x_j}\left[\left(\mu + \frac{\mu_t}{\sigma_\varepsilon}\right)\frac{\partial \varepsilon}{\partial x_j}\right] + \rho C_1\varepsilon S - C_2\rho\frac{\varepsilon^2}{k+\sqrt{\nu\varepsilon}} \tag{6}$$

While $S = \sqrt{2S_{ij}S_{ij}}$ and $S_{ij} = \frac{1}{2}\left(\frac{\partial \bar{u}_i}{\partial x_j} + \frac{\partial \bar{u}_j}{\partial x_i}\right)$.

Where $x_j, \rho, u_i, p, \delta_{ij}, \mu, \mu_t$, $\bar{\tau}_{ij}{}^{lam}$ and $\bar{\tau}_{ij}{}^{turb}$ represent Cartesian coordinate in index notation, density, velocity component, pressure, Kronecker delta, dynamic viscosity, turbulent eddy viscosity, laminar and turbulent Reynolds stress tensor, respectively. The bar represents a time-averaged value. $i, j$ and $k$ represent variables corresponding to one of the three directions, x, y or z independently.

The model constants are:

$C_1 = 1.44$, $C_2 = 1.9$, $\sigma_k = 1.0$, $\sigma_\varepsilon = 1.2$.

The $\mathrm{P}_k = \frac{\bar{\tau}_{ij}{}^{turb}}{\rho}\frac{\partial \bar{u}_i}{\partial x_j}$ is the production term in the turbulent kinetic energy transport equation, while $\sigma_k, \sigma_\varepsilon$, $C_1$, and $C_2$ are the model constants. More details about the mathematical model can be referred to Ansys Fluent Theory Guide[22].

## 2.2. Computational domain and boundary conditions

Figure 1(a) shows the repeated computational domain geometry of each inclined coolant injection hole over a flat plate. The main geometric parameters considered in the simulations are the hole diameter $D = 12.7\ mm$, inclination angle of the hole path $\alpha = 35°$, hole length to diameter ratio $L/D = 4$ and pitch to diameter ratio $P/D = 3$. The computational domain was divided into three sub-domains named: the mainstream fluid domain, injection hole fluid domain, and plenum fluid domain as shown in Fig.1(b). Two non-conformal mesh interfaces are created to connect the three sub-domains.

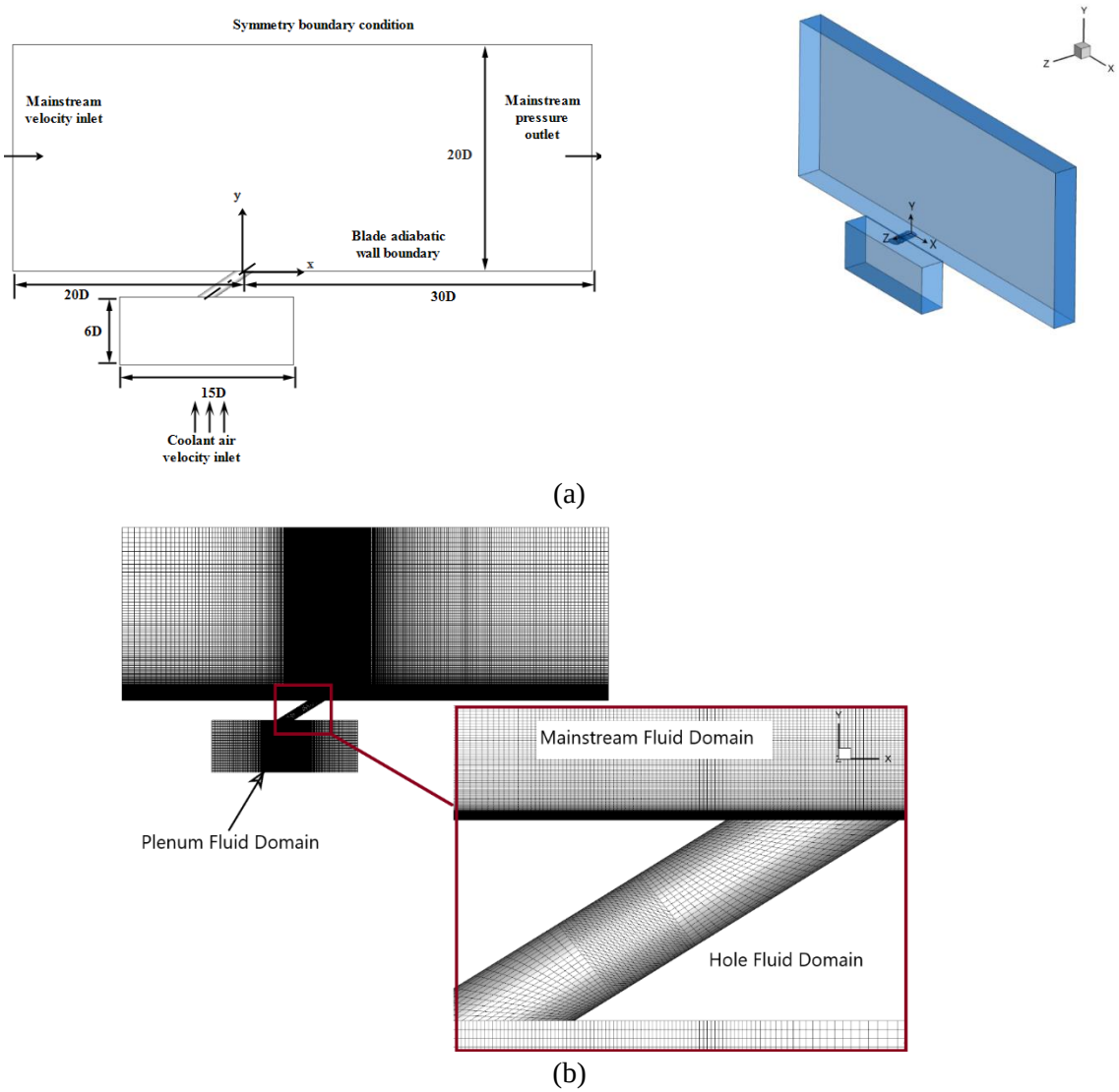


**Fig. 1** (a) Schematic of the computational domain, (b) Mesh generated in the study.

Two cases have been created to perform the study, the first one for a baseline case of film cooling injected from a plain cylindrical hole without a swirl generator. The other one is for the case of film cooling with an in-hole swirl generator with four blades and various geometric parameters considered in the present study. These parameters are the ratio of the swirl generator length to the hole diameter $Ls/D$ (0.8,1.0,1.25), its twist angle $\beta$ (60°,160°,190°), and position in the injection hole path relative

to the path inlet SP (15.4, 20.4, 24.4) mm. Figure 2 shows a schematic of the swirl generator and its geometric parameters used in the model.

The origin of the domain has been chosen at the center of the hole exit in the mainstream and the domain starts upstream at $X = -20D$ , where the velocity inlet boundary is located. The inlet cross-sectional area, $A_m$, is $20D \times 3D$ , and both the inlet temperature $(T_m)$ and velocity $(v_m)$ are considered to be 300 K and 21.6 m/s, respectively. The mainstream fluid domain extends in the x-direction downstream the origin to $X = 30D$ where the pressure outlet boundary is considered to be absolute atmospheric pressure. Away from the injected film cooling and its interaction effects with the mainstream, at $Y = 20D$, the symmetry boundary condition is applied. Periodic boundary conditions are used for the side faces of mainstream and plenum fluid domains at $Z = -1.5D$ and $Z = 1.5D$. The flat plate surface at $Y = 0.0D$ is set as an adiabatic non-slip wall boundary condition. The plenum is located between $Y = -2D$ and $Y = -8D$ with inlet area $Ap = 15D \times 3D$ . This inlet has been considered as a velocity inlet boundary condition with inlet velocity calculated according to the considered blowing ratio $M = (0.5,1.0,1.5,2.0)$. For all considered values of blowing ratios, the temperature of the coolant at the plenum inlet is kept constant at 150 K based on a density ratio $DR$ of 2.0. Finally, the swirl generator parameters inside the injection hole path are defined as depicted in Fig. 2.

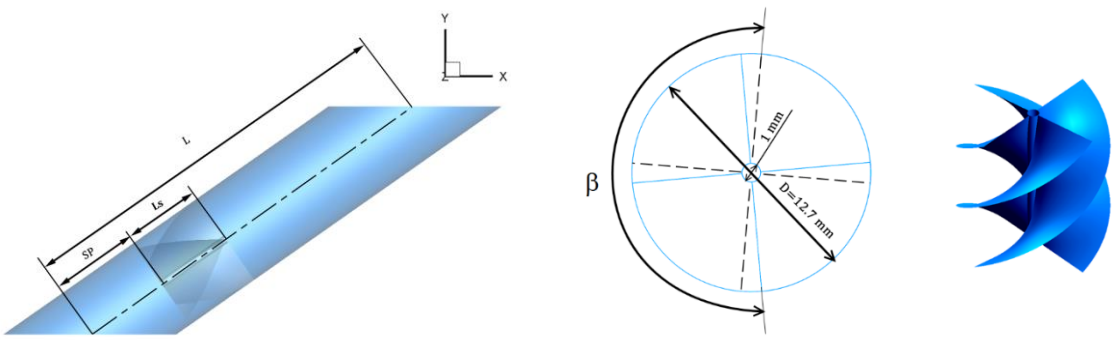


**Fig. 2** Swirl generator characteristics and parameters inside injection hole path

### 2.3. Grid generation and independence test

A structured hexahedral grid is generated which reduces cell count and consequently less memory and time required, also allows the predominant flow to be aligned with the grid. The grid of the mainstream fluid domain and the plenum fluid domain is generated once for all cases and tests. While the grid of the injection hole fluid domain is generated for each geometrical change stated in the test matrix shown in Table (1). From this table, it is shown that for each blowing ratio there are 27 cases due to the variations of the swirl generator length to hole diameter ratio, its twist angle, and position in the injection hole path.

The grid independence test was performed to ensure that increasing the number of grid cells more than the chosen number used in the present computation does not affect the numerical results for all studied cases as shown in Fig.3. The figure shows the centerline effectiveness for the baseline case downstream the injection hole for five cases with different cell numbers at a blowing ratio $M = 1.0$ and density ratio $DR = 2.0$. Apparently, there is no change in results as the number of cells exceeds 3.3 million. Therefore, the number of cells 3.7 million is adopted for the present study. Special care has been given for the mesh in the near wall region to properly model the viscous sublayer with the aid of wall function linked with the used turbulence model.

**Table 1** Test Matrix of the present study.

| Ls/D | 0.8 | | | | | | | | |
|---|---|---|---|---|---|---|---|---|---|
| β (degree) | 60 | | | 160 | | | 190 | | |
| SP (mm) | 15.4 | 20.4 | 24.4 | 15.4 | 20.4 | 24.4 | 15.4 | 20.4 | 24.4 |
| M | 0.5 | 0.5 | 0.5 | 0.5 | 0.5 | 0.5 | 0.5 | 0.5 | 0.5 |
| | 1.0 | 1.0 | 1.0 | 1.0 | 1.0 | 1.0 | 1.0 | 1.0 | 1.0 |
| | 1.5 | 1.5 | 1.5 | 1.5 | 1.5 | 1.5 | 1.5 | 1.5 | 1.5 |
| | 2.0 | 2.0 | 2.0 | 2.0 | 2.0 | 2.0 | 2.0 | 2.0 | 2.0 |
| Ls/D | 1.0 | | | | | | | | |
| β (degree) | 60 | | | 160 | | | 190 | | |
| SP (mm) | 15.4 | 20.4 | 24.4 | 15.4 | 20.4 | 24.4 | 15.4 | 20.4 | 24.4 |
| M | 0.5 | 0.5 | 0.5 | 0.5 | 0.5 | 0.5 | 0.5 | 0.5 | 0.5 |
| | 1.0 | 1.0 | 1.0 | 1.0 | 1.0 | 1.0 | 1.0 | 1.0 | 1.0 |
| | 1.5 | 1.5 | 1.5 | 1.5 | 1.5 | 1.5 | 1.5 | 1.5 | 1.5 |
| | 2.0 | 2.0 | 2.0 | 2.0 | 2.0 | 2.0 | 2.0 | 2.0 | 2.0 |
| Ls/D | 1.25 | | | | | | | | |
| β (degree) | 60 | | | 160 | | | 190 | | |
| SP (mm) | 15.4 | 20.4 | 24.4 | 15.4 | 20.4 | 24.4 | 15.4 | 20.4 | 24.4 |
| M | 0.5 | 0.5 | 0.5 | 0.5 | 0.5 | 0.5 | 0.5 | 0.5 | 0.5 |
| | 1.0 | 1.0 | 1.0 | 1.0 | 1.0 | 1.0 | 1.0 | 1.0 | 1.0 |
| | 1.5 | 1.5 | 1.5 | 1.5 | 1.5 | 1.5 | 1.5 | 1.5 | 1.5 |
| | 2.0 | 2.0 | 2.0 | 2.0 | 2.0 | 2.0 | 2.0 | 2.0 | 2.0 |

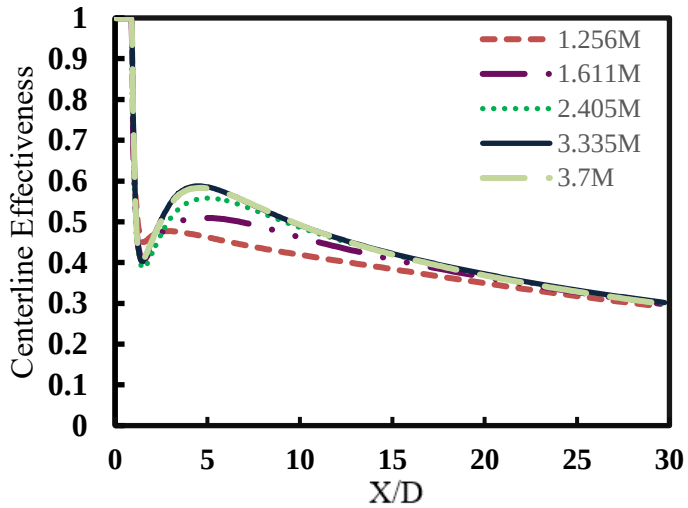


**Fig. 3** Grid independence test

## 2.4. Numerical solution and model validation

ANSYS Fluent release 16.0 CFD solver has been used through the present study in parallel computation mode using double precision and pressure-based solver. Zhang and Hassan [23] presented a comparison between the results obtained using four turbulence RANS models coupled with different near-wall treatments. They postulated that the realizable k-ε turbulence model with the standard wall function shows satisfied agreement with the experimental data. Therefore, the realizable k-ε turbulence model with the standard wall function is utilized to model the present study. The model is solved using second-order upwind scheme for the momentum, energy, and turbulence convective

equations with PRESTO for the pressure correction as indicated in [22] due to the high swirling flow expected in the study. The convergence of the solution has been accepted when the residuals reach an order of magnitude of $10^{-5}$ and the net imbalance is less than 1% of the smallest mass flux in the fluid domain boundary. For the purpose of model validation, the baseline case at a blowing ratio $M = 1.05$ and density ratio $DR = 1.97$ is solved and compared with the experimental study conducted by Pedersen et al. [24] under the same stated operating conditions. Comparison of the obtained computational results of the centerline effectiveness along the hole downstream direction shows a good agreement with the experimental results of [24] as shown in Fig.4.

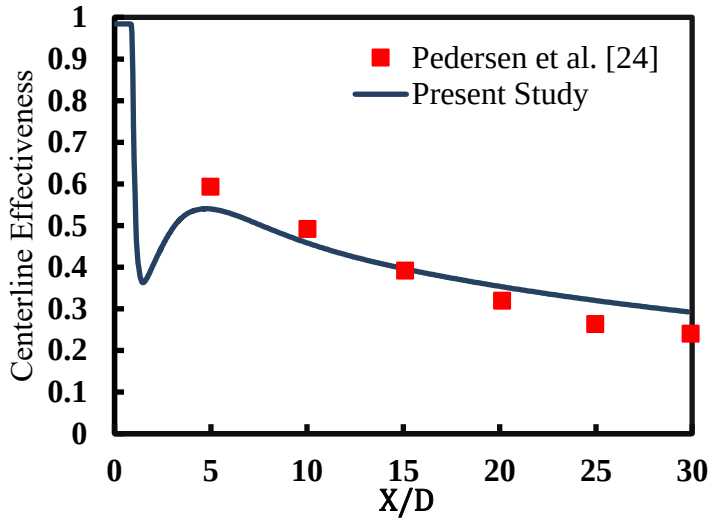


**Fig. 4** Validation of the present study numerical model with the experimental data of Pedersen et al.[24] ($M = 1.05$ , $DR = 1.97$)

## 3. Results and discussion

The results presented and discussed in this section are those obtained for different cases that include studying all parameters arranged in the test matrix shown in Table (1). A total number of 108 cases are studied. These cases considered different swirl generator geometrical parameters and operating conditions. The results are presented and discussed in a manner to show optimum parameters. The steps of optimization start by studying the effect of swirl generator length $Ls/D$ under different blowing ratios $M$, then followed by studying the effect of twist angle $\beta$, and ended by studying the effect of varying the swirl generator position $SP$. The optimization criteria are to determine the parameters which ensure maximum effectiveness uniformity over the flat plate surface at the vicinity of hole and along the downstream direction. Finally, the optimum performance was compared with the baseline case to show the enhancement degree.

### 3.1. Effect of the swirl generator length and blowing ratio.

Figure 5 represents the variation of the laterally averaged film cooling effectiveness along the downstream direction for the case with $\beta = 60°$ and $SP = 15.4$ mm at different values of $Ls/D$ (0.8,1.0,1.25) and blowing ratio $M$(0.5,1.0,1.5,2.0). The figure shows that increasing the blowing ratio at short swirl generator length ($Ls/D$=0.8) leads to a higher laterally averaged film cooling effectiveness near the injection hole. This increase continues up to a certain $X/D$ value that depends on the blowing ratio $M$ then starts to decay. The decay rate increases by increasing the blowing ratio due to high mixing which is expected to occur because of the high swirling intensity level caused by

increasing the blowing ratio. Comparing the results of the three swirl generator lengths $Ls/D$ shown Fig.5, it can be observed that increasing $Ls/D$ causes the cooling jet lift-off. Thus, effectiveness reduction near the injection hole and downstream happens until re-attachment occurs somewhere before $X/D = 5.0$. Furthermore, the intensity of this effect increases as the bowing ratio increases.

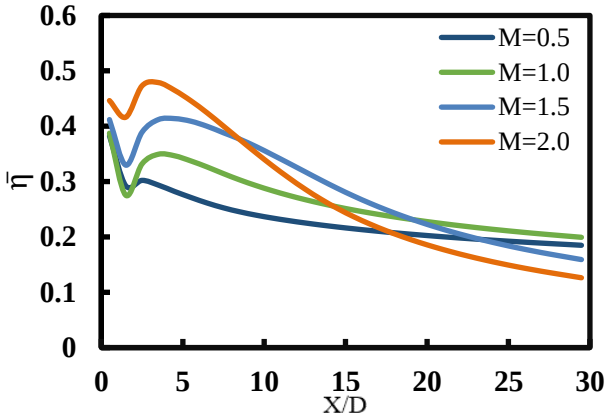


(a) $L_s/D$=0.8

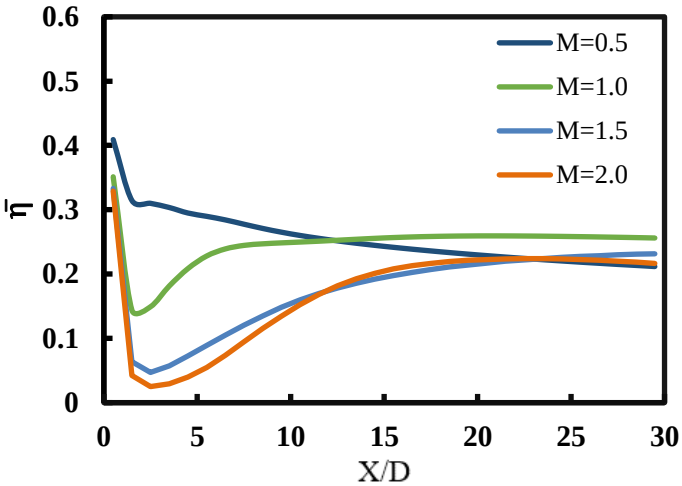


(b) $L_s/D$=1.0

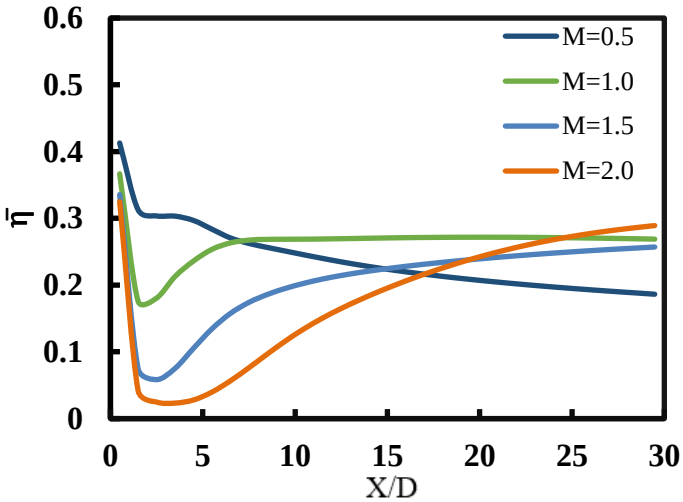


(c) $L_s/D$=1.25

**Fig. 5** Variation of laterally averaged film cooling effectiveness in the downstream direction for a case with β=60°, SP=15.4 mm, at different $M$ and Ls/D values

The swirl parameter $S$ is used to scale the swirl strength and it is defined as the ratio of the circumferential velocity to the axial velocity, $u_\theta/u_{axial}$ , as described in [25]. The jet lift-off is intensified as the swirl number decreases due to an increase in the injected jet axial velocity, which in turn leads to a higher normal-to-wall velocity component. The re-attachment occurs due to the attenuation of the normal-to-wall velocity component and the vortex strength during the penetration of the mainstream flow. From the above results and discussion, the optimum parameters that lead to a relatively uniform laterally averaged effectiveness distribution downstream the hole with no sudden decay or jet lift-off are the shortest swirl generator length $Ls/D$=0.8 accompanied with $M = 1.0$ when $\beta = 60°$ and $SP = 15.4$ mm.

### 3.2. Effect of the swirl generator twist angle

Figure 6 shows the variation of the laterally averaged film cooling effectiveness in the downstream direction for different lengths of the swirl generator $Ls/D$= (0.8,1.0,1.25) when varying the twist angle $\beta = (60°, 160°, 190°)$, while the swirl position and blowing ratio are kept constant at $SP = 15.4$ mm and $M = 1.0$,respectively. In Fig. 6(a), for $Ls/D$=0.8; enhanced jet coverage was observed for all twist angles. However, for twist angle $\beta = 160$ °, higher effectiveness at the vicinity of the hole is observable compared to other values of $\beta$ until $X/D \simeq 8.0$ where it drops down to a lower level than that for the case with twist angle β =60°, but it still has a higher value than β =190°. In addition to that, a steep drop down in effectiveness is obvious for β =190°. Hence, this dropdown is attributed to the excessive mixing that occurs owing to the high swirl strength which causes a large part of the main hot stream to be involved downward by the cooling jet and consequently reducing the effectiveness. Furthermore, the laterally averaged film cooling effectiveness for the case of the twist angle β =60° has a relatively uniform distribution without steep changes from $X/D \simeq 4.0$ to the end of the domain at $X/D = 30$, however, sudden adverse change is discernible in the hole vicinity as the jet lift-off arises. To conclude, the case with $\beta = 160°$ is considered to provide the optimum performance over the other twist angles when it is assessed for hole vicinity along with downstream effectiveness.

In Fig. 6(b, c), at $Ls/D = 1.0$ and 1.25, it is observed that the jet lift-off appeared for the case with $\beta = 60°$. This is attributed to the relatively long swirl generator path that causes a reduction in circumferential velocity, $u_\theta$, of the swirling flow inside the hole. Moreover, this reduction in the $u_\theta$ is accompanied by an increase in the axial jet velocity component hence the jet momentum penetrating the mainstream. In addition to that, it was observed that increasing the twist angle increases the swirl strength level, and this leads to a high mixing and a steep dropdown in the film effectiveness at the twist angle $\beta = 190°$ as shown in Fig. 6(b and c).

By examining the three plots in Fig.6, simultaneously it can be concluded that increasing the swirl generator length $Ls/D$ leads to reduced effectiveness at a constant twist angle. However, a further increase in the twist angle for the same swirl generator length enhances the laterally averaged effectiveness in the region immediately downstream of the injection hole. Additionally, the high swirl strength level causes high mixing which leads to a steep dropdown in the laterally averaged effectiveness, but the swirling coolant jet still has relatively similar coverage near to the domain end. Accordingly, it can be deduced that the best performance accompanies the injection from the hole with swirl generator length to diameter ratio $Ls/D = 0.8$ and a twist angle $\beta = 160°$.

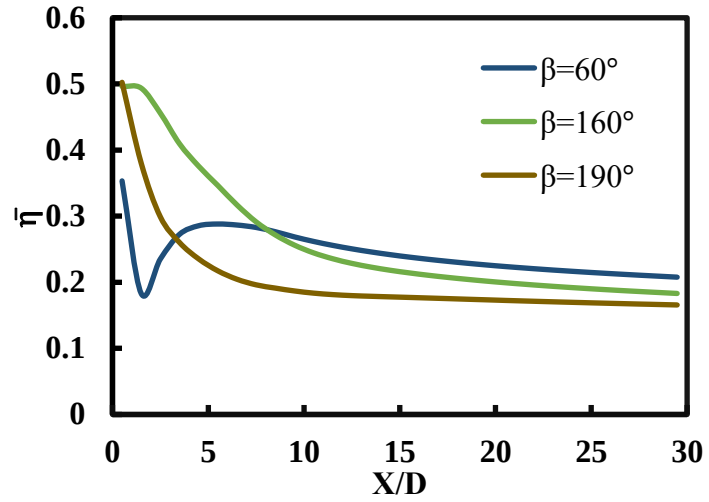


(a) $L_s/D=0.8$

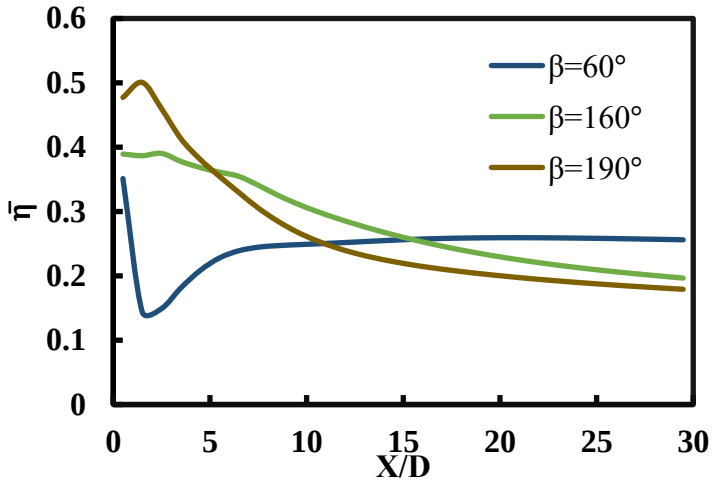


(b) $L_s/D=1.0$

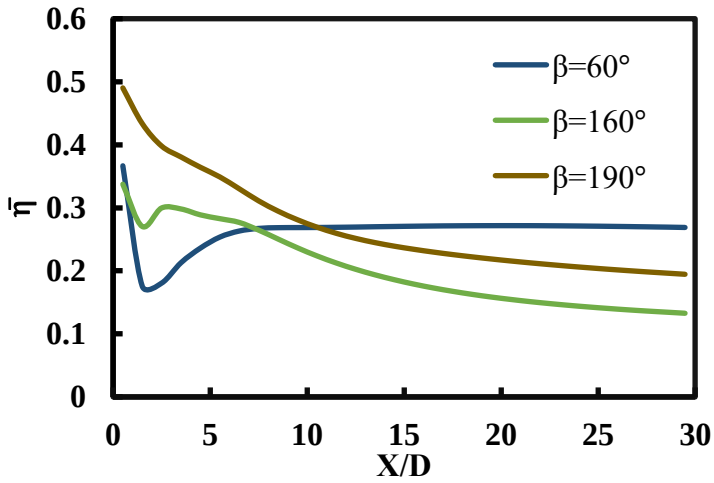


(c) $L_s/D=1.25$

**Fig. 6** Variation of laterally averaged film cooling effectiveness in the downstream direction, for cases of different twist angles and Ls/D at constant SP=15.4 mm and M=1.0

### 3.3. Effect of the swirl generator position

Figure 7 represents the variation of the laterally averaged film cooling effectiveness in the downstream direction for different lengths $Ls/D = (0.8,1.0,1.25)$ while varying the swirl generator position $SP = (15.4, 20.4, 24.4)\ mm$ measured from the inlet section. The swirl generator position is investigated at constant $M = 1.0$, and $\beta = 160°$. In Fig 7 (a) where Ls/D=0.8, it is observed that the coolant jet for the case with a swirl generator position SP=15.4 mm maintains a higher film cooling laterally averaged effectiveness in the hole vicinity until reaching $X/D \leq 5.0$ then it drops down to lower value than the case with SP=20.4 mm. The reason for that is attributed to the stabilizing of the swirling flow after the jet passes the swirl generator due to the long distance as it travels from the swirl generator to the hole exit compared to the other two positions. In addition, this relative long path diminishes the swirling strength and reduces the axial flow momentum package. Therefore, the possibility of jet penetration is reduced, and no detachment is observed. The figure also shows that the position of the generator $SP = 24.4\ mm$ exhibits a detachment of the coolant jet immediately after the hole exit. On the other hand, the swirl generator position SP=20.4 mm maintains a higher uniform distribution of laterally averaged effectiveness for a long downstream distance compared to the other two positions.

Mainly coolant jet lift-off occurs due to the axial momentum goes along with a high swirl strength level. On the other hand, the high angular momentum interaction with the mainstream tends to cause jet reattachment. As shown in Fig. 7(a), the jet reattachment location depends on the swirl generator position such that the closer the swirl generator to the hole exit, the farther the reattachment location downstream the hole. Figures 7 (b) and (c) indicate that the film cooling laterally averaged effectiveness at any downstream location decreases when the swirl generator length is increased. In fact, this is attributed to the increased swirl strength after passing a longer path inside the swirl generator compared to the case of Ls/D = 0.8. For that reason, the jet lift-off is observed for all swirl generator positions in case of the longest swirl generator. Accordingly, it can be stated that the parameters providing the optimum performance for these cases are a swirl generator length to diameter ratio Ls/D=0.8 and a swirl generator position SP=20.4.

### 3.4. Film cooling adiabatic effectiveness.

Figure 8 is a comparison of the film cooling adiabatic effectiveness contours downstream of the film cooling hole with and without a swirl generator at different blowing ratios. The swirl generator used in the comparison has the optimum geometric parameters that provide better coolant coverage with uniform distribution of the cooling effectiveness downstream of the injection hole. As concluded above, these parameters are $Ls/D = 0.8$, $\beta = 160°$, $SP = 20.4$ mm. Figure.8 (a) shows side by side the film cooling effectiveness contours downstream the hole at $M = 0.5$ for the baseline and optimized cases. It is observable that the coolant jet in the case with the swirl generator has a good coverage due to the swirl momentum that reduces the penetration of the cooling jet into the mainstream and increases the lateral diffusion. Symmetric footprint is shown in Fig.8 (a) for the baseline case while an asymmetric footprint of the coolant jet clearly appeared in the case with a swirl generator. The asymmetric jet is a result of the rotation of the coolant flow after passing the swirl generator. More demonstration and explanation of this phenomenon is shown in the next section. Moreover, the jet, in this case, shows superior lateral spreading in the spanwise direction, compared to the baseline case, particularly as the blowing ratio increases as shown in Figs 8 (b) and (c).

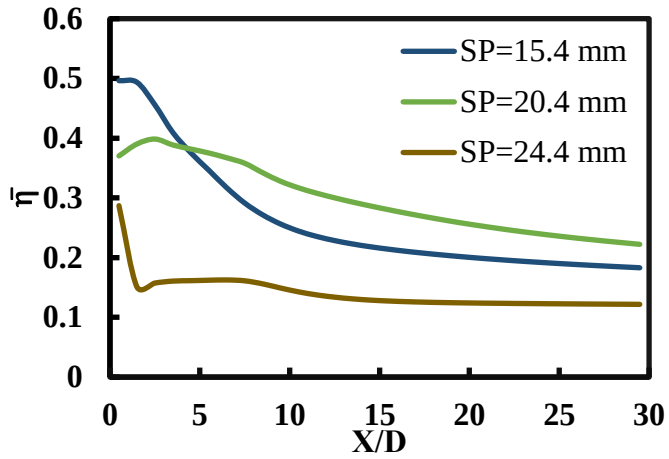


(a) $L_s/D=0.8$

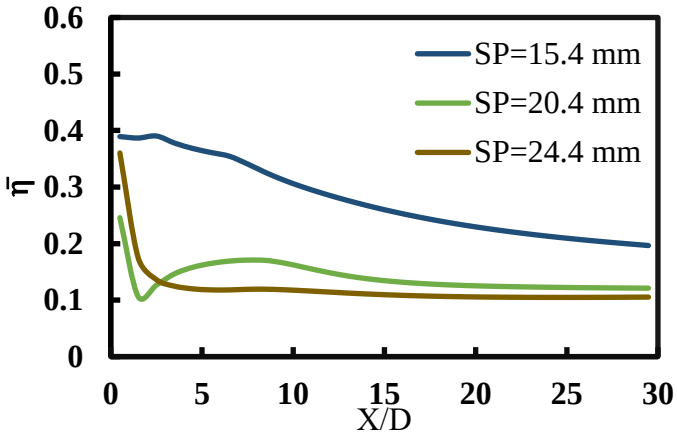


(b) $L_s/D=1.0$

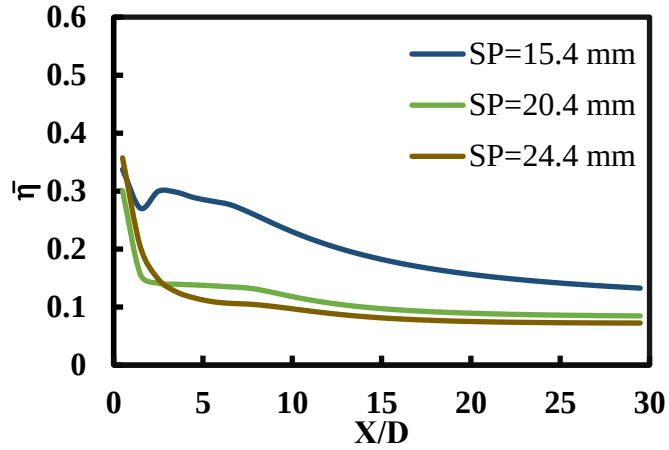


(c) $L_s/D=1.25$

**Fig.7** Variation of laterally averaged film cooling effectiveness in the downstream direction, at different swirl position and Ls/D values at constant β=160° and M=1.0

Moreover, it is observable from the figure that for the case with a swirl generator there is a low effectiveness region between two high effectiveness zones downstream of the injection hole which results in a hairpin shape of the effectiveness contours as shown clearly in Fig. 8(b). This figure shows that the hairpin leg in the negative *z* direction maintains higher effectiveness till the end of the domain

while the other hairpin leg's effectiveness has a higher decay rate and is bent in the positive $z$ direction.

The deflection of the cooling jet shown in Fig. ٨(b) and (c) at $M = 1.0$ and $M = 2.0$,respectively, in the positive $z$ direction is expected to be a result of the Coriolis force accompanying the rotating flows. As indicated in[26], Coriolis force is a type of volume force like inertia and centrifugal forces which affect each fluid particle. These forces have a significant effect on the characteristics of the rotating (swirling) flows which cannot be ignored. Coriolis force is defined in terms of the angular and linear velocity of the flow as given in [25] by:

$$F_{Cor} = -2\rho\omega \times V \tag{7}$$

The rotation direction of the generated swirling flow in the present scheme is counter- clockwise because of the pitching of the swirl generator blades. This rotation direction causes the deflection of the coolant jet in the positive $z$ direction because of generated Coriolis force which acts on the fluid particles in the right direction relative to the coolant jet. As Eq. (7), shows the strength of Coriolis force and consequently the jet deflection increases when the velocity increases which is achieved by increasing the blowing ratio as Fig. 8(b) and Fig. 8(c) show.

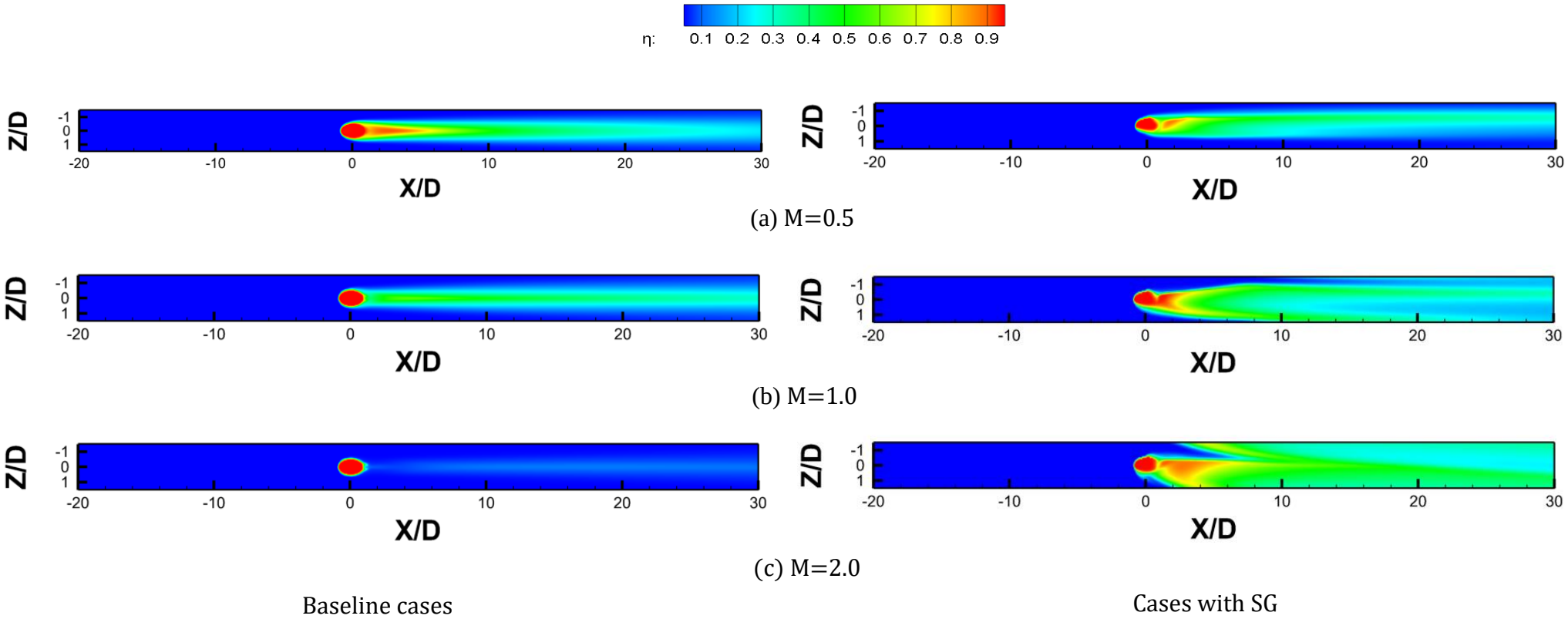


**Fig. 8** Comparison of the adiabatic film cooling effectiveness in the downstream direction for a case of *Ls/D=0.8, β=160° SP=20.4 mm* and baseline case at different blowing ratios

Figure (9) shows a quantitative comparison of laterally averaged film cooling effectiveness at different downstream locations for the case with optimum parameters and baseline case at different blowing ratios. At a blowing ratio of $M = 0.5$ , Fig. 9(a), it is apparent that there is not a much difference between the performances of both cases particularly away from the coolant injection hole. However, slightly enhanced effectiveness is observable for the baseline case in the near-hole region compared to the case with a swirl generator. Increasing the blowing ratio to $M = 1.0$ and $M = 2.0$ enhances the performance of the case with a swirl generator compared to corresponding baseline case at both blowing ratios. Such performance enhancement is attributed to the absence of jet lift-off, while the performance of the corresponding baseline cases goes down due to jet lift-off and digestion of the jet by the mainstream hot gas flow. Figure 9(c) shows that there is a sudden rise of the laterally averaged film cooling effectiveness followed by a steep change at $M = 2.0$ immediately downstream of the injection hole compared to the more uniform effectiveness distribution accompanying the case at $M = 1.0$ as shown in Fig.9(b).

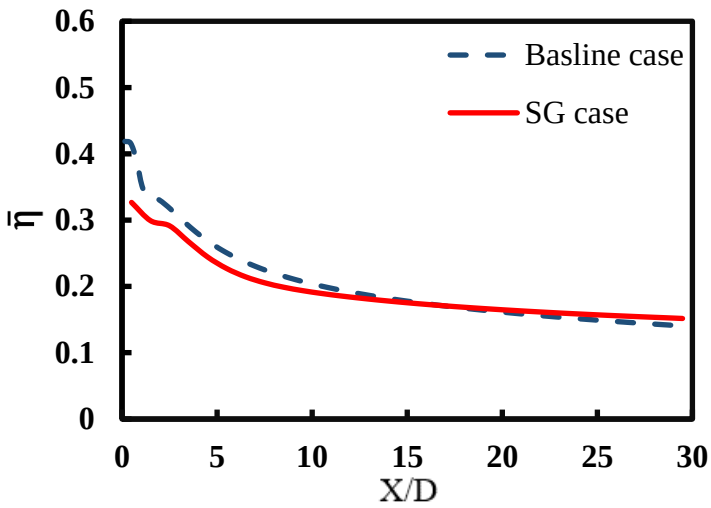


(a) M=0.5

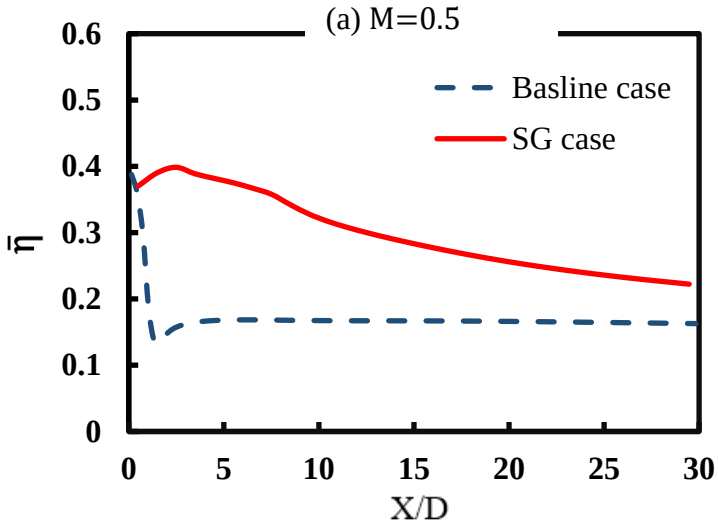


(b) M=1.0

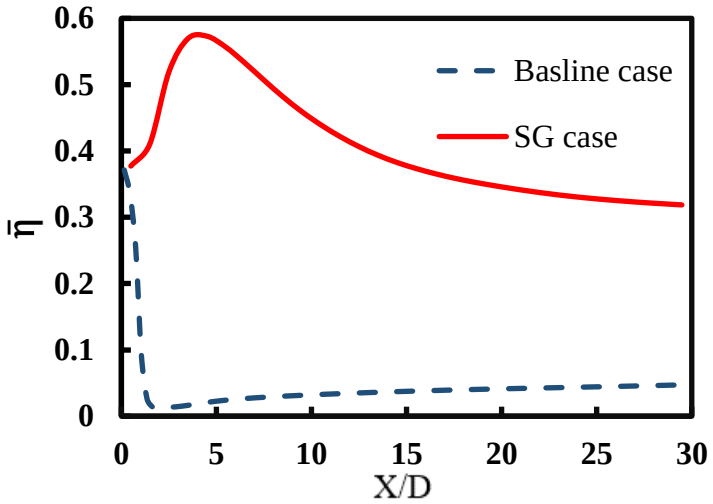


(c) M=2.0

**Fig. 9** Comparison of laterally averaged film cooling effectiveness in the downstream direction for the case of optimum parameters and baseline case at different blowing ratios

### 3.5. Flow field characteristics downstream of the injection schemes

An assessment is performed to examine the characteristics of new vortices generated due to adding the swirl generator inside the film cooling hole compared to the regular CRVP that generated by the baseline case without swirl generator. Figure 10 shows the temperature contours and the streamline patterns at different downstream locations of $X/D = 1.5$, $3.0, 6.0,$ and $10.0$ at a constant blowing ratio, $M = 1.0$ for both the baseline case and the case with the swirl generator. For the baseline case, Fig. 10(a) shows clearly the kidney shape vortex pair and the vortex core expansion along the downstream direction. The shear layer developed due to the interaction of the mainstream and the coolant jets that results from the difference in both streams' velocities leads to a rolling up of the CRVP. This, in turn, leads to the digestion of the hot stream under the coolant jet and lift-off occurrence as shown in the figure, particularly as $X/D$ increases.

Fig. 10(b) shows that there are three new vortices generated in the flow field because of adding the swirl generator inside the injection hole. The first one is a one of the CRVP that enriched by adding the swirl generator blades pitching and exists near the middle of the flow field with a counterclockwise rotation direction. The figure indicates that it also has the dominant effect in the flow field. The other two vortices are a right side up-vortex induced by the dominant swirl vortex and a left side down-vortex is the other CRVP with both having clockwise rotation directions. This set of rotation directions leads to a unidirectional flow in the interface regions between the two vortices and the middle largest vortex as presented in Fig. 10. The direction of the flow between the large-middle vortex and the up-right vortex is in the upward direction acting as a resisting curtain to turn aside the hot gas particles from penetrating the coolant jet. This describes why the left side hairpin leg of the cooling effectiveness, appearing in Fig. 8(b), maintains a good adhesion with the wall and consequently keeps higher effectiveness values to the end of the investigated domain.

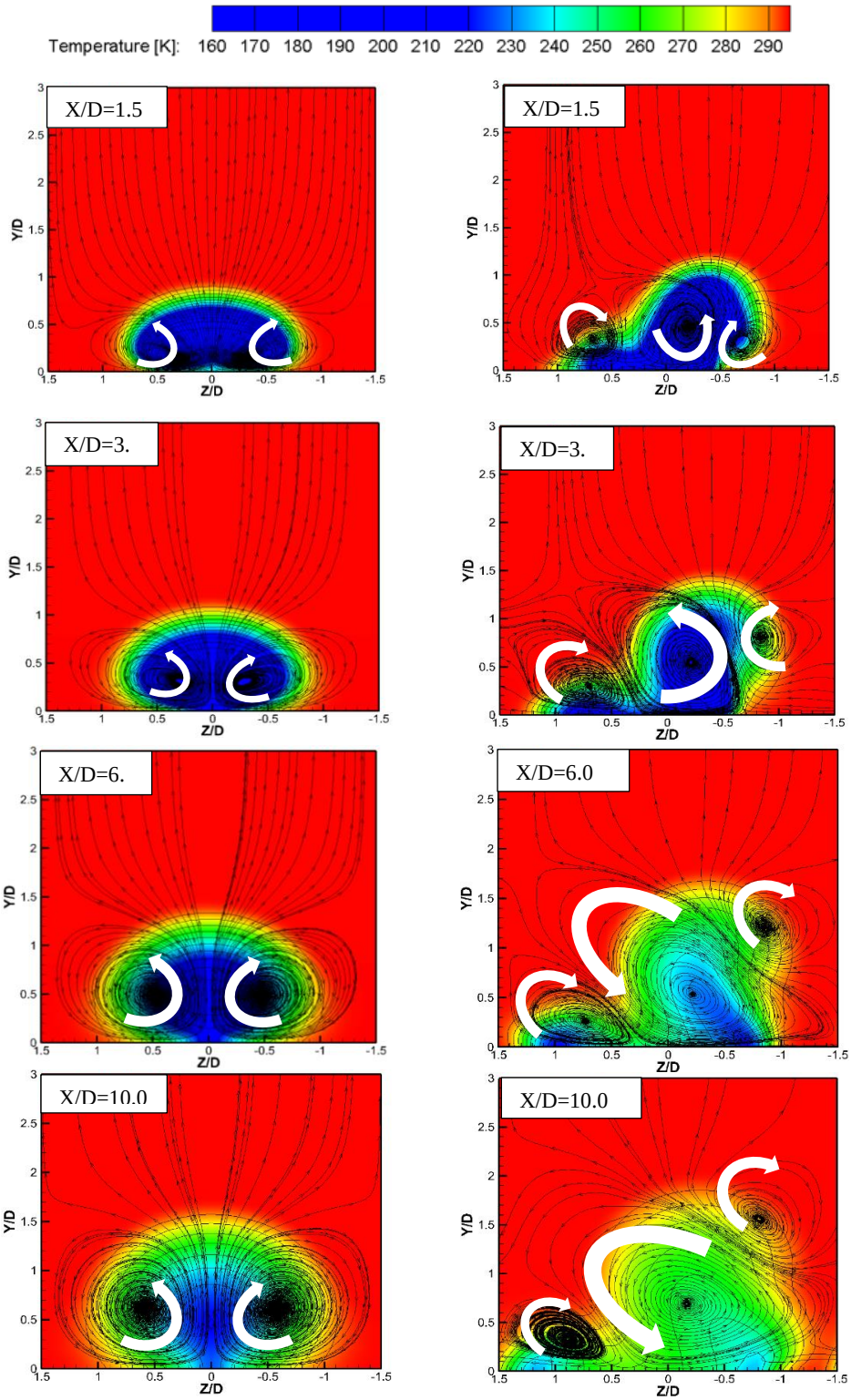


(a) Baseline case (b) Case with SG

**Fig.10** Temperature contour and streamlines pattern at different downstream locations at M=1.0 (a) baseline (b) case with Ls/D=0.8, β=160° and SP=20.4 mm

The direction of the flow in the interface region between the large-middle vortex and the down-left vortex is a downward direction leading to the digestion of the hot gas stream inside the coolant jet. The involvement of the hot gas, between the two vortices, explains the lower

effectiveness values taking place in the middle region between the two regions of the high effectiveness values forming the legs of the hairpin footprint as described above and shown in Fig. 8 (b). This effect vanishes with increasing the amount of the injected coolant. The center of the large-middle vortex moves slowly away from the negative $z$ direction to the positive $z$ direction with the downstream location as shown in Fig. 10(b). While its movement, it compresses the left down-vortex and makes it deformed and displaced in the positive $z$ direction resulting in a good jet adhesion to the wall. The interaction between the right up-vortex core and the large-middle vortex moves it upwards and drifts slightly towards the positive z-axis region and this interaction pulls the small vortex in its way upward to a certain location. Once this location is reached, the growing of the right-up vortex causes deformation and deflection of the large middle vortex in the positive $z$ direction.

Figure 11 shows the contours of vorticity $\omega_x$ at different downstream locations in the y-z plane for the same cases and condition represented in Fig.10. The vorticity $\omega_x$ of the optimum case has extremely high values compared to the baseline case. A symmetrical vorticity is observed in the baseline case while asymmetrical vorticity is observed in the optimum case with a swirl generator. The vorticity contours of the optimum case shows that the core of the vortex having positive vorticity values is moving from the negative z-axis to the positive z-axis while expanding along the downstream direction. This observation agrees with the above discussion of the path of the large middle vortex which results in compressing the down-left vortex and causing a good jet adhesion to the wall.

Figure 12 shows a comparison of temperature plots for optimum case with SG and the baseline case without SG at $M = 1.0$. This figure mainly shows entrainment of the coolant jet into the mainstream. For Fig.12 (a) of the baseline case a light blue region of temperature appears under a dark blue immediately downstream the hole outlet which indicates to the jet lift off phenomena. While it clearly appears in Fig. 12 (b) that a dark blue region touches the surface downstream of the hole outlet, that means the coolant jet has no evidence of jet lift off in the new scheme. However, the thickness of the interaction region between jet and the mainstream in fig. 12 (b) is larger than that in fig. 12 (a) which indicates to the large-scale vortex developed in the new scheme because of adding SG. Another observation is that temperature in the core of the jet has a significant drop in downstream direction for the optimum case compared to the baseline case and that is a result of high mixing accompanies the large-scale vortex.

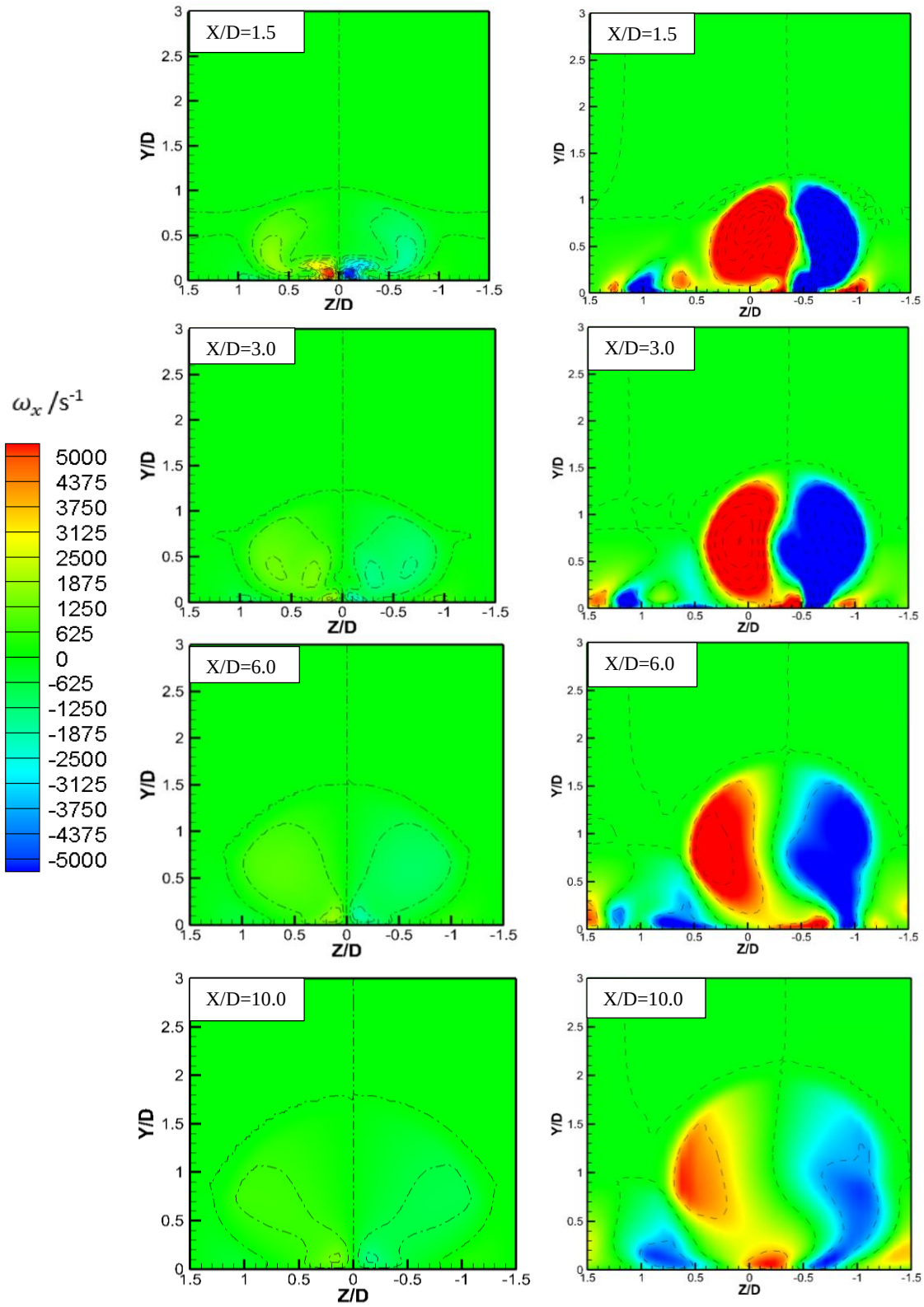


**Fig. 11** Vorticity contoı (a) Baseline case ownstream locat (b) Case with SG ine (b) case with Ls/D=0.8, β=160° and SP=20.4 mm

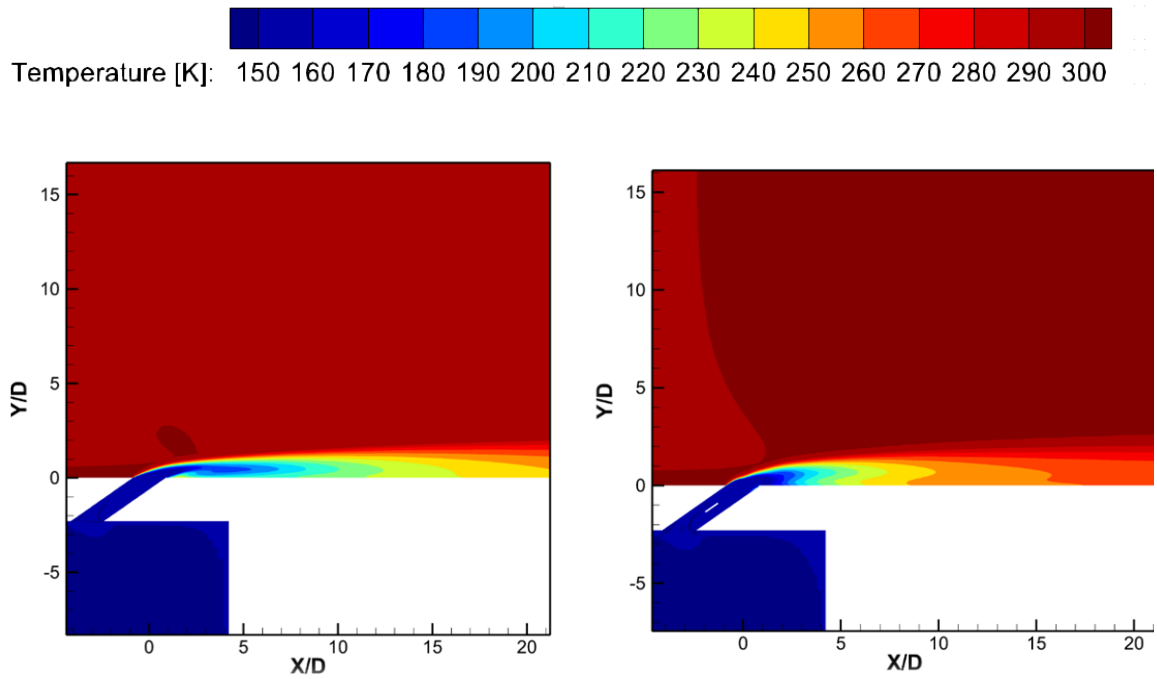


(a) Baseline (b) Optimum Case with SG

**Fig. 12** Temperature contours at $Z/D = 0$ , and M=1.0 (a) baseline (b) optimum case with Ls/D=0.8, β=160° and SP=20.4 mm

Figure 13 represents a comparison of velocity contours in x-direction with streamlines at two positions in the hole for the baseline case and the optimum case with SG at $M = 1.0$. For Fig. 13 (a) two vortices appear in near hole inlet plot at $Y = -2.0\,D$ and thus separation occurs in the hole entrance while the streamlines look more coherent in the near hole outlet plot at $Y = -0.4\,D$ as the flow develops, and the vortices attenuates. For Fig. 13 (b) the streamlines pattern at $Y = -2.0\,D$ are similar to same plot of the baseline case while they are more rotational and have some vortices in near hole outlet at $Y = -0.4\,D$. And this describes the cause of the large scale-vortex that appears downstream the hole exit.

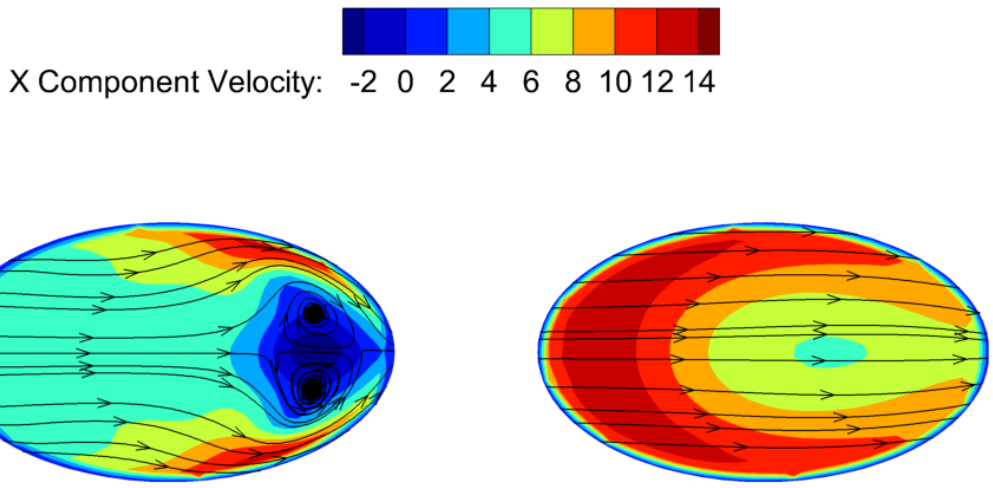


Surface at $Y = -2.0\,D$ , After hole inlet Surface at $Y = -0.4\,D$, Before hole outlet

(a) Baseline Case

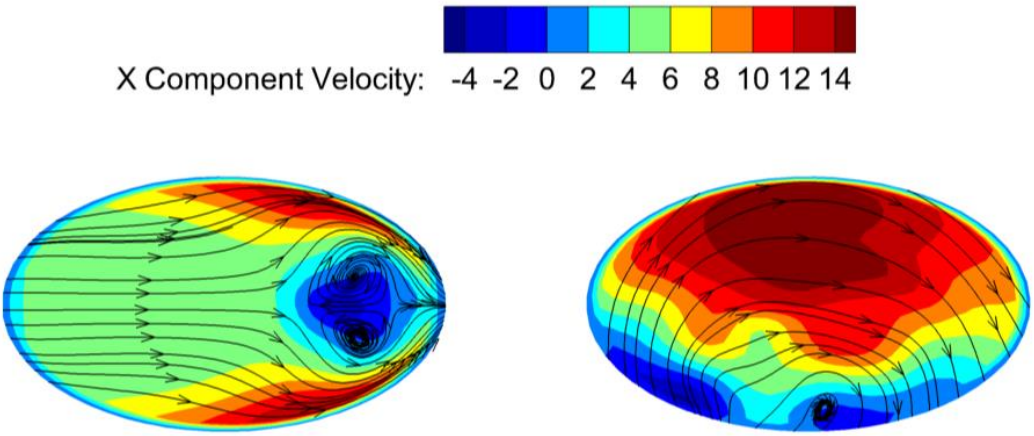


Surface at $Y = -2.0\ D$ near hole inlet  Surface at $Y = -0.4\ D$, Before hole outlet

(b) Optimum Case with SG

**Fig. 13** Velocity in x-direction contours with streamlines at two positions in the hole, and M=1.0 (a) baseline (b) optimum case with Ls/D=0.8, β=160° and SP=20.4 mm

### 3.6. Cooling uniformity coefficient

As the maximum laterally averaged effectiveness uniformity is utilized to optimize the swirl generator geometrical parameters, the Cooling Uniformity Coefficient, that was introduced by Javadi [27], is employed as a quantitative index to quantify effectiveness enhancement. The CUC is calculated using the following formula [27]:

$$CUC = 1 - \frac{|\bar{\eta} - \eta_c|}{\eta_c} \tag{8}$$

Figure 14 (a) shows a comparison of CUC, laterally averaged, and centreline film cooling effectiveness for the baseline case without the SG at $M = 1.0$. As depicted in this figure, the CUC is low in the region downstream of the cooling hole due to jet lift-off, then it increases as the jet expands after $X/D = 5.0$, and the jet reattaches to the surface again.

Figure 14 (b) shows a comparison of CUC, laterally averaged, and centreline film cooling effectiveness for the optimum case with the SG at $M = 1.0$. The CUC shows that the presence of the SG resulted in superior cooling uniformity downstream the injection hole specifically after $X/D = 8.0$ where the values of CUC are between 0.9 to 1.0. Rapid enhancement in the CUC is observable in the region where$X/D < 8.0$ compared to the baseline case while there are two fluctuating points after $X/D = 8.0$. These fluctuations are raised because of overlapping between the centreline effectiveness and the laterally averaged effectiveness curves where their values are equal at these locations. To conclude, the cooling uniformity of the SG scheme is much better compared to the circular hole scheme under the same operating conditions.

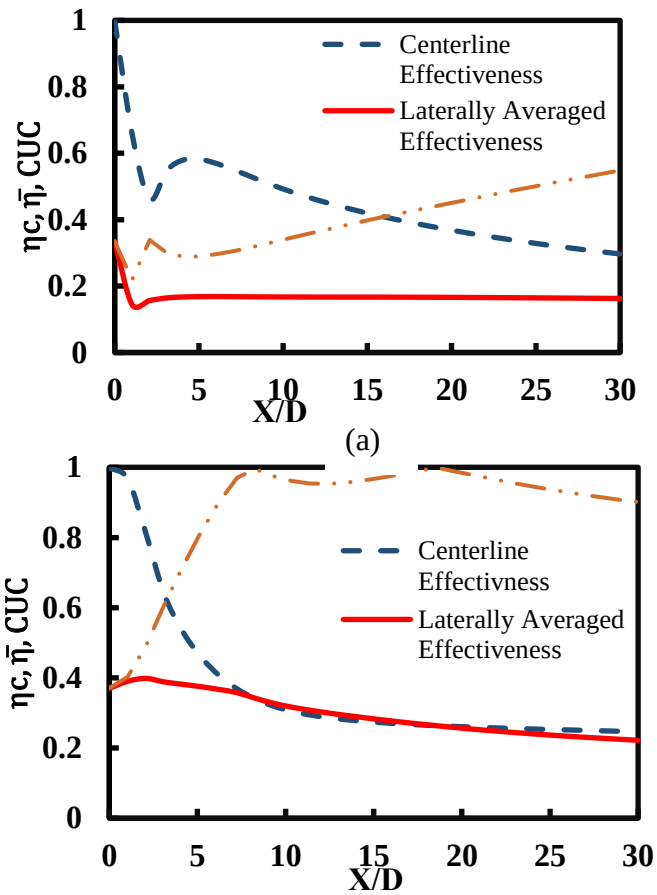


**Fig.14** Centreline effectiveness, CUC, and la r averaged film cooling effectiveness at M=1.0 (a) baseline (b) case with Ls/D=0.8, β=160°, and SP=20.4 mm

### 3.7. Effect of adding the swirl generator on pressure drop and discharge coefficient.

The total pressure drop is one of the crucial effects that may affect the use of swirl generator inside the cooling injection holes. During the present study, both total pressures drop due to insertion of swirl generator inside the injection hole path and due to the interaction of the cooling jet with the mainstream are investigated. Figure 15(a) represents the averaged total pressure at two locations: at the hole inlet and exit, for both cases with and without swirl generator. From the figure shown, the pressure drop can be calculated by Eq. (9), therefore the total pressure drop of case with SG equals 429.065 [Pa], and the total pressure drop of the baseline case equals 104.315 [Pa]. Based on that, the ratio of the total pressure drop of SG case to the baseline case is 4.113.

$$\Delta P = P_1 - P_2 \tag{9}$$

On the other hand, Figure 15 (b) shows the averaged total pressure drop across the mainstream because of the presence of injection holes with and without SG. In the same way as the previous calculation of the total pressure drop ratio, the ratio here is 0.857 which means the total pressure drop in the mainstream of the SG case is less than the pressure drops of the baseline case. Somehow the new scheme facilitates the interaction of the jet and the mainstream. Hence, the

aerodynamic performance will not be affected by the presence of the new scheme, however there is a slight improvement compared to the baseline.

The discharge coefficient $C_d$ is one of the essential parameters that turbine designers pursue to know to evaluate the film cooling performance for different geometries and flow conditions Hay et al. [28]. Therefore, $C_d$ is calculated to benchmark the performance of the new SG scheme to the cylindrical hole scheme. Table 2 shows the values of the $C_d$ for the baseline case and the optimum SG case at $M = 1.0$. For the case of SG, the $C_d$ is lower than that of the baseline case since the new scheme incorporates an extra flow loss like the losses resulting from swirl existence within the hole.

**Table 2** Discharge Coefficient of the baseline case and the optimum SG case.

| | Baseline case | Optimum SG case |
|---|---|---|
| $C_d$, [-] | 0.6768 | 0.4366 |

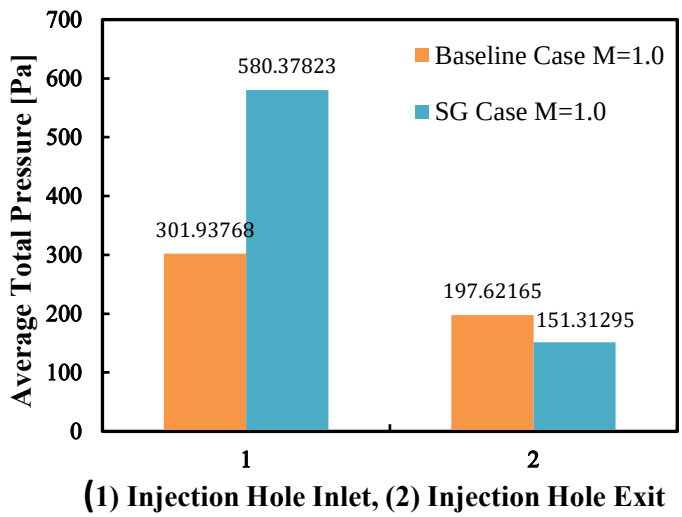


(a) Injection Hole

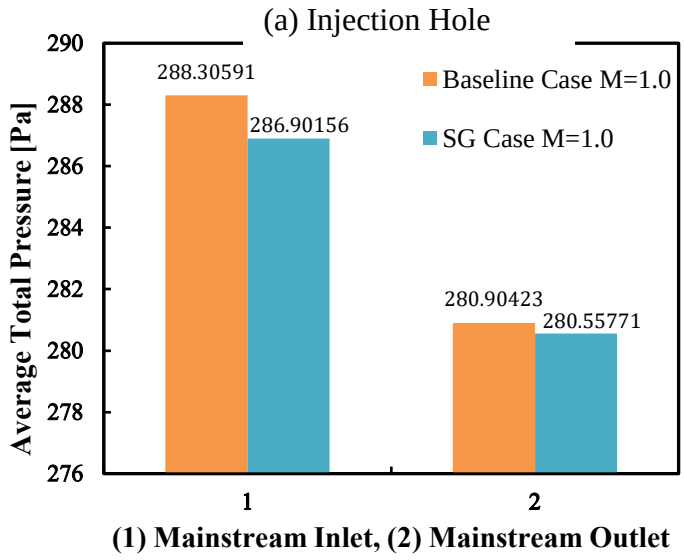


(b) Mainstream

**Fig.15** Average total pressure for both baseline and optimum SG cases at M=1.0 and two regions in the domain (a) Injection Hole (b) Mainstream

## 4. Conclusion

A new film cooling scheme is proposed to enhance cooling performance of gas turbine blades. This scheme incorporates a blade-type swirl generator to add a swirl pattern in the injected coolant stream. The temperature field and the flow field of multiple swirl generator configurations are numerically investigated and compared to the cylindrical hole scheme. The obtained results of the new scheme show better coverage of coolant over the surface in the hole vicinity and downstream the hole compared to cylindrical hole. The area-averaged cooling effectiveness increased by 74%, 293%, and 805% at blowing ratios 1.0, 1.5 and 2.0, respectively, compared to that for a cylindrical hole scheme.

From obtained results, the following concluding remarks could be derived:

1- **The geometrical parameters** of the swirl generator have a significant effect on its film cooling performance. Increasing the swirl generator length to hole diameter ratio $Ls/D$ reduces film cooling effectiveness. Longer generators create more coherent swirl flow, leading to jet lift-off and reduced effectiveness. An optimal twist angle of 160 degrees enhances cooling performance and uniformity. Finally, placing the swirl generator in the middle of the cooling hole path outperforms other locations.

2- **The flow field characteristics** show a new vortical structure induced by the swirl generator while no presence of the CRVP. The vortical structure consists of three main vortices, the large middle vortex, the up-right vortex, and the down-left vortex. A unidirectional flow in the interface of these vortices forms the footprint of the coolant jet on the blade surface. The new vortical structure mainly directs coolant toward the surface while shielding it from the harsh mainstream flow.

3- **The total pressure drop** through the hole and the mainstream are appraised in the present study. The new scheme increases pressure drop through the hole, but slightly improves mainstream aerodynamic performance compared to the baseline case.

## 5. Future Perspective

A plan is established to conduct further numerical simulations and wind tunnel experiments in the future to explore a more comprehensive design of the in-hole swirl generator. Moreover, we will delve deeper into understanding of how swirling flow mechanisms influence the cooling performance by presenting and discussing some other parameters such as swirl parameter, Heat Transfer Coefficient HTC, Net Heat Flux Reduction NHFR, Nusselt number, and more. Manufacturing aspects and real-world implementation of this scheme is a central topic to be studied in the future.

## References

1. Acharya S, Kanani Y (2017) Chapter Three - Advances in Film Cooling Heat Transfer. In: Sparrow EM, Abraham JP, Gorman JM (eds) Advances in Heat Transfer Elsevier, pp. 91-156.
2. Goldstein RJ (1971) Film Cooling. In: Irvine TF, Hartnett JP (eds) Advances in Heat Transfer Elsevier, pp. 321-379.
3. Bunker RS (2005) A Review of Shaped Hole Turbine Film-Cooling Technology. Journal of Heat Transfer 127: 441-453 DOI 10.1115/1.1860562

4. Bogard DG, Thole KA (2006) Gas Turbine Film Cooling. Journal of Propulsion and Power 22: 249-270 DOI 10.2514/1.18034
5. Leylek JH, Zerkle RD (1994) Discrete-Jet Film Cooling: A Comparison of Computational Results With Experiments. Journal of Turbomachinery 116: 358-368 DOI 10.1115/1.2929422
6. Fric TF, Roshko A (2006) Vortical structure in the wake of a transverse jet. Journal of Fluid Mechanics 279: 1-47 DOI 10.1017/S0022112094003800
7. Haven BA, Kurosaka M (1997) Kidney and anti-kidney vortices in crossflow jets. Journal of Fluid Mechanics 352: 27-64 DOI 10.1017/S0022112097007271
8. Kusterer K, Bohn D, Sugimoto T, Tanaka R (2006) Double-Jet Ejection of Cooling Air for Improved Film Cooling. Journal of Turbomachinery 129: 809-815 DOI 10.1115/1.2720508
9. Heidmann JD, Ekkad S (2008) A Novel Antivortex Turbine Film-Cooling Hole Concept. Journal of Turbomachinery 130 DOI 10.1115/1.2777194
10. Dhungel A, Lu Y, Phillips W, Ekkad SV, Heidmann J (2009) Film Cooling From a Row of Holes Supplemented With Antivortex Holes. Journal of Turbomachinery 131 DOI 10.1115/1.2950059
11. Ely MJ, Jubran BA (2009) A numerical evaluation on the effect of sister holes on film cooling effectiveness and the surrounding flow field. Heat and Mass Transfer 45: 1435-1446 DOI 10.1007/s00231-009-0523-8
12. Ely MJ, Jubran BA (2009) A Numerical Study on Improving Large Angle Film Cooling Performance through the Use of Sister Holes. Numerical Heat Transfer, Part A: Applications 55: 634-653 DOI 10.1080/10407780902821532
13. Ming Li H, Hassan I (2015) The Effects of Counterrotating Vortex Pair Intensity on Film-Cooling Effectiveness. Heat Transfer Engineering 36: 1360-1370 DOI 10.1080/01457632.2015.1003715
14. Kuya Y, Nuntadusit C, Ishida H, Momose K, Kimoto H (2004) An Application of Swirling Jet to Film CoolingThe Proceedings of the Thermal Engineering Conference, pp. 283-284.
15. Takeishi K, Oda Y, Egawa Y, Kitamura T (2010) Film cooling with swirling coolant flowWIT Transactions on Engineering Sciences, pp. 189-200.
16. Oda Y, Takeishi K, Shimizu D (2011) Large eddy simulation of film cooling with swirling coolant flowASME/JSME 2011 8th Thermal Engineering Joint Conference, AJTEC 2011 American Society of Mechanical Engineers.
17. Yang W, Pu J, Wang J (2015) Combination effects of upstream-ramp and swirling coolant flow on film cooling characteristicsProceedings of the ASME Turbo Expo American Society of Mechanical Engineers (ASME).
18. Yang X, Liu Z, Liu Z, Feng Z (2015) Numerical analysis on effects of coolant swirling motion on film cooling performance. Int J Heat Mass Transf 90: 1082-1089 DOI 10.1016/j.ijheatmasstransfer.2015.07.055
19. Thurman D, Poinsatte P, Ameri A, Culley D, Raghu S, Shyam V (2016) Investigation of spiral and sweeping holes. Journal of Turbomachinery 138: 091007 DOI 10.1115/1.4032839
20. Yue G, Dong P, Jiang Y, Gao J, Zheng Q (2017) Research on film cooling mechanism of vortex reconstruction induced by swirling coolant flowProceedings of the ASME Turbo Expo American Society of Mechanical Engineers (ASME).
21. Jia Y, Liu Y, Meng Z, Yin W, Hua W (2023) Numerical study on film cooling effectiveness from spiral-channel hole. International Communications in Heat and Mass Transfer 143: 106716 DOI https://doi.org/10.1016/j.icheatmasstransfer.2023.106716
22. Ansys®Fluent., Release16.0. (2015) Theory Guide ANSYS, Inc., Canonsburg, PA.
23. Zhang XZ, Hassan I (2006) Film cooling effectiveness of an advanced-louver cooling scheme for gas turbines. J Thermophys Heat Transfer 20: 754-763 DOI 10.2514/1.18898
24. Pedersen DR, Eckert ERG, Goldstein RJ (1977) Film cooling with large density differences between the mainstream and the secondary fluid measured by the heat-mass transfer analogy. Journal of Heat Transfer 99: 620-627 DOI 10.1115/1.3450752

25. Tan CS, Greitzer EM, Graf MB (2004) Swirling flow. In: Tan CS, Greitzer EM, Graf MB (eds) Internal Flow: Concepts and Applications Cambridge University Press, Cambridge, pp. 389-445.
26. Shevchuk IV (2016) Overview of Rotating Flows. In: Shevchuk IV (ed) Modelling of Convective Heat and Mass Transfer in Rotating Flows Springer International Publishing, Cham, pp. 1-9.
27. Javadi K (2018) Introducing Film Cooling Uniformity Coefficient. Heat Transfer Engineering 39: 180-193 DOI 10.1080/01457632.2017.1288056
28. Hay N, Lampard D (1998) Discharge Coefficient of Turbine Cooling Holes: A Review. Journal of Turbomachinery 120: 314-319 DOI 10.1115/1.2841408